**PAPER** • **OPEN ACCESS**

# Investigation of pressure-driven superconductivity in $TlInTe_2$: an *ab initio* study

To cite this article: Christopher Renskers and Elena R Margine 2024 *Phys. Scr.* **99** 085962

Physica Scripta

OPEN ACCESS

RECEIVED
3 May 2024

REVISED
7 June 2024

ACCEPTED FOR PUBLICATION
19 June 2024

PUBLISHED
18 July 2024



PAPER

# Investigation of pressure-driven superconductivity in $TlInTe_2$: an *ab initio* study

**Christopher Renskers and Elena R Margine***

Department of Physics, Applied Physics, and Astronomy, Binghamton University-SUNY, Binghamton, NY, 13902, United States of America

* Author to whom any correspondence should be addressed.

**E-mail:** crenske1@binghamton.edu **and** rmargine@binghamton.edu

**Keywords:** first-principles calculations, superconductivity, electron-phonon coupling, phonon-mediated superconductor

Supplementary material for this article is available online

## Abstract

The Zintl compound $TlInTe_2$ is an intriguing material because of its outstanding thermoelectric properties at ambient pressure. Interestingly, it has recently been found that $TlInTe_2$ exhibits a V-shape dependence of the superconducting critical temperature ($T_c$) under increasing pressure, which has been linked to the reversed behavior of the Raman active $A_g$ phonon mode and anharmonic effects. In this study, we have performed first-principles calculations of the electron-phonon interactions and the superconducting properties of $TlInTe_2$ in order to understand this unusual pressure-induced response. In contrast to experiment, we find a dome-shaped pressure-induced dependence of $T_c$ with a maximum value of 0.23 K at 18 GPa, significantly lower than the experimental results. Electron doping has the potential to adjust the $T_c$ to fall within the experimental range, but it necessitates considerably high levels of doping. Furthermore, our analysis of the phonon spectra and phonon lifetimes, including anharmonic effects, show that anharmonicity is unlikely to influence the superconducting properties of $TlInTe_2$. It remains an open question whether there is indeed an unusual V-shape $T_c$ dependence with pressure or whether the phonon-mediated theory of superconductivity used here breaks down in this system.

## 1. Introduction

Chain crystal structures from the TlSe family, such as $TlInSe_2$, $TlGaTe_2$, and $TlInTe_2$, exhibit exciting properties at ambient pressure [1–4]. For example, $TlInTe_2$ has an exceptionally low value of lattice thermal conductivity (~0.5 W/mK at room temperature) [5], and $TlInSe_2$ is considered to have outstanding thermoelectric properties [6]. However, relatively limited research has been conducted on this material class under pressure [7–10].

According to the first high-pressure Raman study on $TlInTe_2$ performed by S Ves in 1990, it was suggested that a structural transition from the tetragonal to hexagonal phase may occur in the 7-17 GPa range, but the type of symmetry in the new phase could not be determined [7]. The next work, conducted 30 years later, used Raman spectroscopy, x-ray diffraction, and transport measurements along with first-principles crystal structure prediction to investigate pressure-induced structural and electronic transitions [10]. It was found that the system undergoes a superconducting transition at 5.7 GPa with a reported critical temperature ($T_c$) of 3.8 K. Further compression resulted in a decrease in the critical temperature to a minimum of 2.9 K at 10 GPa, followed by an increase to a maximum observed value of 4.3 K at 25 GPa. This V-shape behavior of $T_c$ was correlated with the pressure dependence of the Raman active $A_g$ mode, where the $T_c$ decreases (increases) as the $A_g$ mode hardens (softens), respectively.

The potential role of the $A_g$ mode is compelling because it is well known that, at ambient conditions, $TlInTe_2$ is an anharmonic system, where the anharmonicity is considered to be responsible for the ultra low value of the lattice thermal conductivity [1, 5, 11–13]. Additionally, a recent theoretical study employing a minimal model of superconductivity that takes into account the anharmonic decoherence of the optical phonons predicted a non-

monotonic behavior of $T_c$ under pressure, in qualitative agreement with the V-shape curve observed experimentally [14].

The focus of this *ab initio* study is to analyze the structural, electronic, vibrational, and superconducting properties of $TlInTe_2$ as a function of pressure. First, we show that the tetragonal phase remains dynamically stable within the 0-30 GPa range, consistent with the latest experiments [10]. Second, in stark contrast to the experimental results that found a V-shaped pressure-induced dependence of $T_c$, we find a dome-shaped pressure-induced dependence with a maximum $T_c$ value of 0.23 K at 18 GPa, approximately 20 times smaller than the largest experimental value. To further understand this discrepancy, we investigated the effect of anharmonicity on both the phonon dispersion and the phonon lifetimes at 0 and 14 GPa. Our theoretical results show that, at 0 K, the anharmonic renormalization of the harmonic phonon frequencies is negligible and the low-frequency phonons have extremely high lifetimes, which suggest that anharmonic effects should play a minor role in the superconducting properties of $TlInTe_2$. We also analyzed the effect of doping and found that $T_c$ values in the experimental range could, in principle, be reached but only for large doping levels.

## 2. Methods

First-principles calculations were carried out with the Quantum ESPRESSO (QE) package [15, 16]. We employed the optB86b-vdW functional [17–21] and optimized norm-conserving Vanderbilt pseudopotentials (ONCVPSP) [22] from the Pseudo Dojo library [23] generated with the relativistic Perdew–Burke–Ernzerhof parametrization [24]. The $5d^{10}6s^26p^1$ orbitals for Tl, $4d^{10}5s^25p^1$ for In, and $4d^{10}5s^25p^4$ for Te were included as valence electrons. A plane wave kinetic-energy cutoff of 80 Ry for the wavefunctions and 400 Ry for the charge density and potential were used. For the Brillouin-zone integration of the 8-atom unit cell, we used a Γ-centered $12 \times 12 \times 12$ **k**-mesh [25] with a Methfessel–Paxton smearing [26] width of 0.01 Ry. The atomic positions and lattice parameters were optimized until the total energy was converged within $10^{-6}$ Ry and the force on each atom was less than $10^{-4}$ Ry/Å. The dynamical matrices and the linear variation of the self-consistent potential were computed using density-functional perturbation theory (DFPT) [27] on the irreducible set of a regular $4 \times 4 \times 4$ **q**-mesh. The electron-phonon (e-ph) interactions were first evaluated on a Γ-centered $12 \times 12 \times 12$ **k**-mesh and an irreducible set of a regular $4 \times 4 \times 4$ **q**-mesh. For each **q**-point, the e-ph matrix elements were linearly interpolated to a denser $60 \times 60 \times 60$ **k**-mesh [28].

The EPW [29–31] code was used to investigate the e-ph interactions and estimate the critical temperature for select pressures. The electronic wavefunctions required for the Wannier-Fourier interpolation [32, 33] were calculated on a Γ-centered $8 \times 8 \times 8$ **k**-mesh. Thirty maximum localized Wannier functions ($sp^3$ hybridized orbitals for Tl, In, and Te) were used to describe the electronic structure. Uniform $60 \times 60 \times 60$ **k**-point and $30 \times 30 \times 30$ **q**-point grids were employed in the e-ph coupling calculations.

Anharmonic effects can be computed through approaches based on stochastic sampling, *ab initio* molecular dynamics, explicit computation of higher order interatomic force constants (IFCs), or special displacements [34–42]. Here, the ALAMODE package [39, 43, 44] was used to compute anharmonic phonon frequencies and phonon linewidths through the real-space supercell apporach employing a $2 \times 2 \times 2$ supercell of 64 atoms. This required the extraction of the second-, third-, and fourth-order IFCs. The second-order IFCs were extracted by performing displacements of 0.01 Å for atoms in the supercell and computing the Hellmann-Feynman forces for the displaced configuration. The anharmonic third- and fourth-order IFCs were extracted in a similar way as the second-order terms but with a displacement of 0.04 Å. There were no cutoff radii specified for the computation of the second- and third-order terms, including all interactions, however, the fourth-order term used a cutoff radius to only include nearest neighbor interactions for every atomic pair. The IFCs that contain a combination of atoms whose pair is larger than the cutoff radius is set to zero. The fitting error for the fourth-order IFCs was 0.20% at 14 GPa. Setting the nearest neighbor distances up to 8 Bohr required the calculation of over 800 displacements. Using the default distance of 10 Bohr would have significantly increased the computational cost and would have required calculating over 3500 displacements for a 64 atom unit cell. Considering the substantial computational cost for a larger cutoff radius, and the small fitting error achieved for nearest neighbors, the use of the smaller cutoff seems appropriate in this case. The anharmonic phonons were obtained by solving the self-consistent phonon (SCPH) equation. Both the **q**-mesh and the inner **q**′-mesh in the SCPH were set to $4 \times 4 \times 4$. The phonon linewidths were calculated by taking the imaginary part of the anharmonic self-energy on a $10 \times 10 \times 10$ **q**-mesh.

## 3. Crystal properties

At ambient conditions, $TlInTe_2$ adopts the tetragonal crystal structure, with space group $I4/mcm$ (No. 140) [45]. The unit cell consists of covalently bonded tetrahedral chains of [$InTe_2$] along the *c*-axis, as shown in figure 1

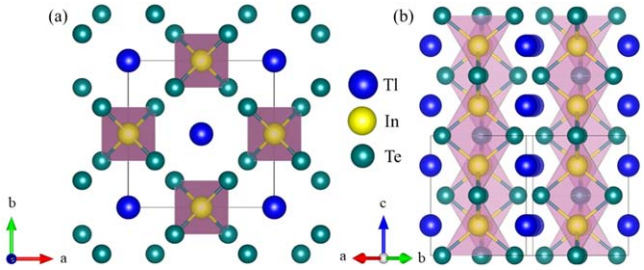


**Figure 1.** (a) Top and (b) side view of the tetragonal crystal structure of $TlInTe_2$. The In-Te polyhedra enclose the weakly bonded Tl in the structure.

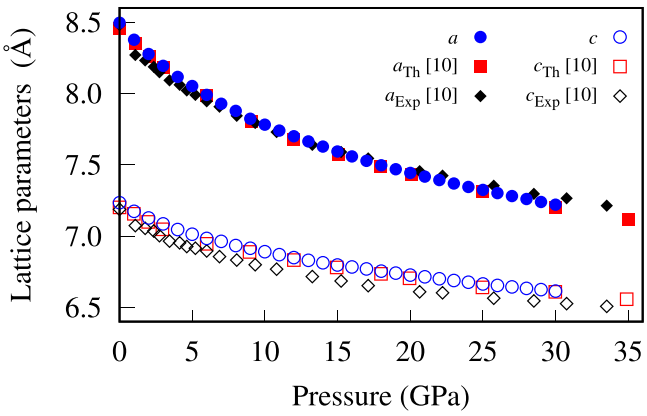


**Figure 2.** Lattice parameters along *a* (filled symbols) and *c* (open symbols) axes as a function of pressure. Blue circles correspond to results from this work, while red squares and black diamonds correspond to theoretical and experimental results from [10].

[46]. The tetrahedrons connect to each other by the corner shared Te atoms, with the In atom residing in the middle of the tetrahedron. The Tl atoms occupy the center of a distorted octagon formed by 8 Te atoms (2 different side lengths), with the Tl and Te atoms ionically bonded. The weak bonding of the Tl atoms is characteristic of rattler structures where loosely bound atoms in a regular periodic crystal lattice have large amplitude vibrations. The rattling model has been demonstrated in $TlInTe_2$ [5] and shown to be typical for materials with low lattice thermal conductivity [47, 48].

A possible tetragonal to hexagonal structural phase transition in the 7-17 GPa range was pointed out in [7], but the Raman measurements did not allow for the determination of the symmetry in the new phase. On the other hand, a recent study did not find any evidence of a phase transition from the x-ray diffraction patterns taken up to 33.5 GPa, but predicted that the tetragonal structure undergoes a phase transition to a body-centered cubic $Pm\bar{3}m$ phase at 50 GPa through an intermediate distorted orthorhombic *Pbcm* phase that appears at 37.5 GPa [10]. We find that the tetragonal structure indeed remains dynamically stable up to 30 GPa, the maximum pressure investigated in our work, consistent with the latest study [10]. In addition, as shown in figure 2, the present theoretical results for the pressure dependence of in-plane and out-of-plane lattice parameters are in very good agreement with the theoretical and experimental data reported in [10], confirming that there is no structural phase transition in the 0-30 GPa pressure range.

## 4. Electronic properties

According to experimental measurements, $TlInTe_2$ is a semiconductor with an indirect band gap of approximately 1.0 eV [49–51], and undergoes a semiconductor-to-semimetal transition at 4 GPa [10]. Our density functional theory (DFT) calculations return a lower band gap value of 0.29 eV and a semiconductor-to-semimetal transition at 2 GPa, as expected within the PBE scheme employed in this work. We also carried out electronic structure calculations with the modified Becke-Johnson (MBJ) exchange-correlation potential [52] that has been shown to provide a good description of band gaps in crystalline solids. With MBJ, we find that the band gap increases to 0.71 eV, in agreement with previous DFT calculations [10, 53, 54], and the semiconductor-

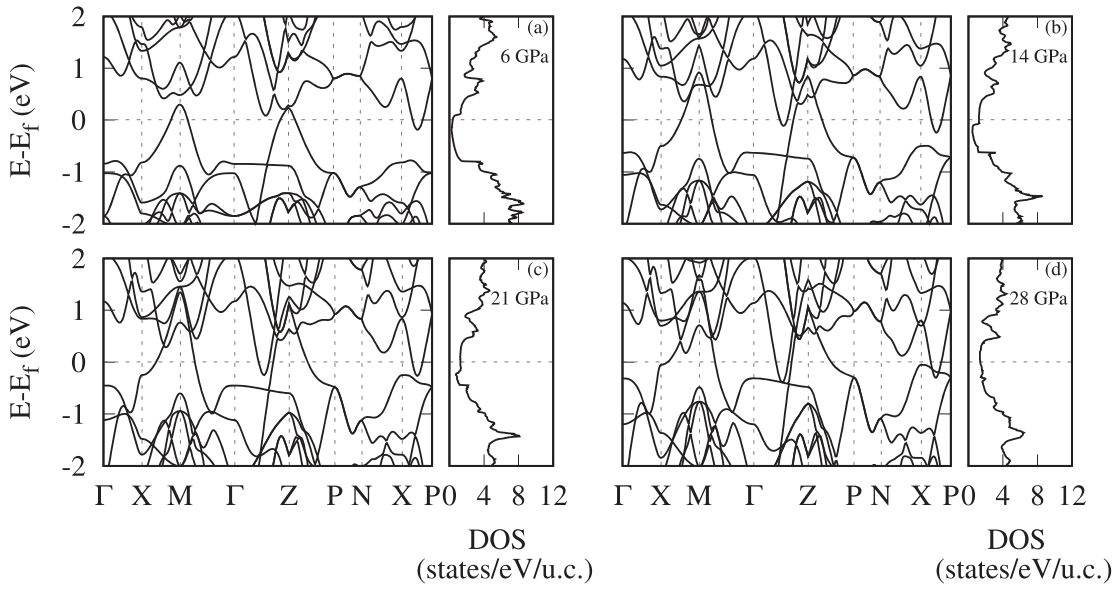


**Figure 3.** Calculated electronic band structure and density of states (DOS) of $TlInTe_2$ at (a)-(d) 6, 14, 21, and 28 GPa.

to-semimetal transition shifts to 4 GPa. However, the role of the MBJ potential is secondary when describing the electronic structure in the vicinity of the Fermi level ($E_F$) in metallic systems.

To confirm this, we performed band structure calculations at 0 GPa (semiconducting) and 24 GPa (metallic), with and without the MBJ potential. As shown in figure S1 in the Supplemental Material [55], the MBJ potential at 0 GPa does a good job of reproducing the band features of the PBE calculation while shifting the conduction and valence bands away from the Fermi level. Meanwhile, at 24 GPa, there is no appreciable difference in the band structure near the Fermi level. As a result, the density of states (DOS) at the Fermi level for the two sets of calculations are almost identical for pressure points where the system is in the metallic regime. Lastly, band structure calculations at 0 and 24 GPa with the inclusion of spin–orbit coupling (SOC) indicate that the SOC has a negligible effect (see figure S1 in the Supplemental Material [55]). Since our primary interest is to investigate the superconducting properties of $TlInTe_2$, which is predominately influenced by the electronic structure at the Fermi level, we performed all subsequent calculations at the PBE level without the inclusion of SOC.

The evolution of the electronic band structure and total DOS as pressure increases from 6 to 28 GPa is depicted in figure 3. At 6 GPa, the valence and conduction bands cross the Fermi level in the vicinity of the *M* and *Z* high-symmetry points and along the *X*-*P* direction, respectively. Around 14 GPa, the conduction band along the Γ-*Z* direction is also pushed down below the Fermi level, and the valence and conduction bands start to overlap. This results in an over two fold increase in the DOS at $E_F$. Past this point, the DOS changes very little with increasing pressure. From the projected DOS (see figure S2 in the Supplemental Material [55]), we infer that in the 6-28 GPa pressure range, the main contribution at the Fermi level comes from Te 5*p*, In 5*s*, and Tl 6*p* states. Our band structure results are in good agreement with previous electronic calculations both at ambient and high pressure [10, 54].

Next, we investigated the effect of pressure on the Fermi surface topology of $TlInTe_2$ [56]. In a number of systems [57–61], the emergence or disappearance of superconductivity has been associated with a Lifshitz transition [62]. This transition is manifested as a subtle change in the Fermi surface topology (e.g., the appearance or disappearance of a pocket or a neck on the Fermi surface) driven by external parameters, such as doping or pressure, and without breaking the crystal symmetry. Our theoretical analysis clearly shows that the crystal structure remains the same up to 30 GPa, but the topology of the Fermi surface evolves as a function of pressure, as shown in figure S3 in the Supplemental Material [55]. We observe that at 6 GPa the Fermi surface is comprised of individual electron and hole pockets. As pressure increases, the electron pockets connect and grow tubular necks forming an umbrella-shaped Fermi surface. It has been proposed that the appearance of these tubular necks could be responsible for the onset of superconductivity in $TlInTe_2$ [10].

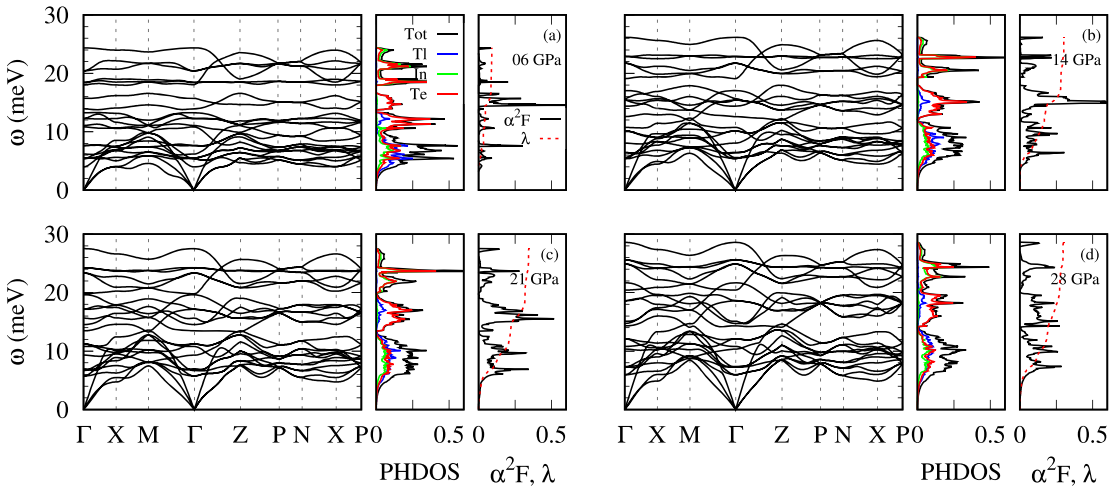


**Figure 4.** Calculated phonon dispersion, phonon density of states (PHDOS), isotropic Eliashberg spectral function ($\alpha^2F(\omega)$), and electron-phonon coupling strength ($\lambda$) of $TlInTe_2$ at (a)-(d) 6, 14, 21, and 28 GPa. The total PHDOS (black line) is decomposed with respect to the vibrations of the Tl (blue line), In (green line), and Te (red line) atoms.

## 5. Vibration and electron-phonon properties

Figure 4 displays the calculated phonon dispersion and atomic projected phonon density of states (PHDOS) at 6, 14, 21, and 28 GPa. The partial decomposed PHDOS shows that the spectrum can be separated into three frequency regions with different atomic contributions. The low-frequency region up to about 10 meV is linked to vibrations from all three types of atoms. The intermediate-frequency region from approximately 10 to 20 meV has little to zero contribution from the lighter In atoms and is characterized almost entirely by Te vibrations. The high-frequency region above 20 meV has evenly mixed contributions from the In and Te atoms with no contribution from the heavier Tl atoms. As pressure increases, there is a general hardening of all phonon branches across the Brillouin zone, except for the $A_g$ Raman active mode that has a dome-shaped dependence, peaking around 10 GPa, as shown in figure S4 in the Supplemental Material [55]. Our results capture well the pressure trends of the $A_g$ and $E_g$ modes observed experimentally, the former being slightly downshifted by about 1-2 meV. This level of underestimation is comparable to the one found for the $A_g$ mode in other systems [63, 64].

We further analyze the Eliashberg spectral function, $\alpha^2F(\omega)$, and the e-ph coupling strength, $\lambda$, in conjunction with the PHDOS. The comparison between $\alpha^2F(\omega)$ and PHDOS in figure 4 shows that, for all calculated pressures, the modes below 15 meV are responsible for more than two thirds of the total e-ph coupling strength of the system. The remaining third mainly comes from the intermediate-frequency modes of Te, with only a small part from the high-frequency modes of In and Te. We note that in the intermediate region lies the aforementioned Raman active $A_g$ mode whose dome-shaped frequency dependence and its broadening linewdith as pressure increases has been suggested to lead to strong e-ph coupling and anharmonicity, and therefore was used to explain the V-shape $T_c$ behavior as a function of pressure extracted from transport measurements in [10]. Based on the calculated $\lambda$, we find that the $A_g$ mode does not play a major role in the e-ph coupling in $TlInTe_2$. In addition, it has been shown that the strong anharmonicity in this material is linked to the low-frequency rattling mode of Tl atoms [5, 12], and, from the projected PHDOS, we see that the $A_g$ mode is mainly associated with the vibration of the Te atoms. Our anharmonic calculations presented later also show that the $A_g$ mode does not appear to be influenced by anharmonic effects. Figure 5 summarizes the dependence of the DOS at the Fermi level and $\lambda$ as a function of pressure. Compression, from 6 to 15 GPa, results in an increase in $\lambda$ as the DOS at the Fermi level increases. Past this pressure point, the general hardening of all phonon modes triggers a decrease in $\lambda$. The corresponding critical temperatures estimated with the Allen-Dynes modified McMillian formula [65, 66] and a Coulomb pseudopotential of $\mu^* = 0.1$ using QE are shown in figure 5(c). Superconductivity calculations for select pressures performed with EPW give similar $\lambda$ and $T_c$ values. We find that $TlInTe_2$ does not exhibit superconductivity until 10 GPa, and the $T_c$ only reaches a maximum value of 0.23 K at 18 GPa. These results differ from the experimental findings in two significant ways: the V-shape curve of superconductivity is not recovered and the critical temperature is off by an order of magnitude.

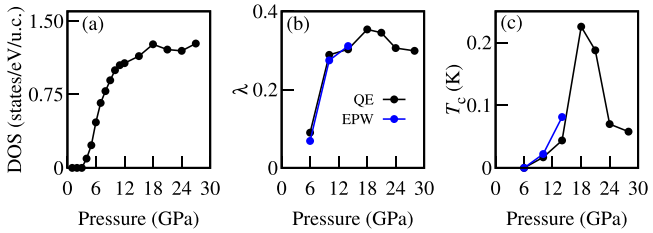


**Figure 5.** (a) DOS at the Fermi level, (b) electron-phonon coupling strength ($\lambda$), and (c) critical temperature ($T_c$) for pressures ranging from 0 to 28 GPa. The black circles correspond to calculations done with QE, while the blue circles were calculated with EPW.

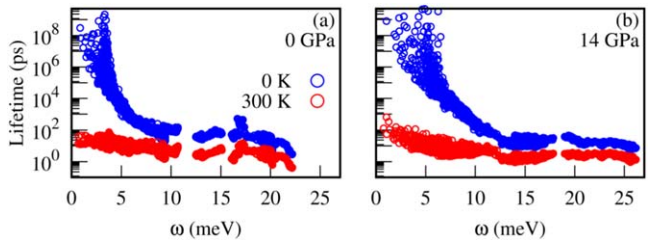


**Figure 6.** Phonon lifetimes at (a) 0 GPa and (b) 14 GPa calculated at 0 K (blue circles) and 300 K (red circles).

## 6. Discussion

The significant anharmonicity in the rattling motion of Tl atoms enclosed within the cage-like Thompson cubes formed by surrounding Te atoms has been proven to be a major contributor to the remarkably low lattice thermal conductivity observed in $TlInTe_2$ [1, 5], as it results in ultra-low phonon lifetimes [12, 13]. To this end, we calculated the phonon frequencies including quartic anharmonic effects within the SCPH theory. As shown in figure S5 in the Supplemental Material [55], the phonon spectra at 14 GPa computed within the harmonic approximation with DFPT in QE and frozen-phonon in ALAMODE are found to be in good agreement. Taking into account aharmonic effects, we observed that the phonons between 5 and 20 meV are slightly hardened with increasing temperature, while the high-frequency optical phonons remain relatively unchanged, in agreement with calculations at 0 GPa in [12]. These findings suggest that anharmonic effects are not expected to affect the superconducting properties of $TlInTe_2$. To further support this point, we also calculated the phonon lifetimes at 0 and 300 K for 0 and 14 GPa. The comparison in figure 6 demonstrates that the lifetimes of low-frequency phonons at 0 K are much larger than those at 300 K for both pressure values. Since smaller lifetimes are linked to anharmonic effects, this plot implies that while $TlInTe_2$ might be strongly anharmonic at room temperature, the anharmonicity is dampened at low temperatures.

We further explored whether doping could enhance the superconducting transition temperature and bring the results in line with experimental observation. We simulated electron doping using a jellium model for two carrier densities of 0.25 and 0.50 electrons/u.c. Figures S6 and S7 in the Supplemental Material [55] show the band structures and phonon dispersion relations for the doped compound at 6, 10, 14, and 21 GPa. Across all pressures, the DOS at $E_F$ for the smaller doping remains comparable to the undoped compound. This behavior changes for the higher doping as a new state crosses the Fermi level along the $N$-$X$ direction, leading to a more than 25% increase in the DOS at $E_F$. In the case of phonons, there is a general softening of all modes which becomes more pronounced as doping increases. The cumulative effect of the increase in the DOS at the Fermi level and the softening of the phonon modes results in a significant enhancement of the predicted e-ph phonon coupling and critical temperature. As shown in figure 7, the calculated $T_c$ is of the same order of magnitude as the experimental value, but the $T_c$ dependence with pressure does not display the V-shape behavior found experimentally, instead decreasing almost linearly with increasing pressure independent of the doping concentration. Pressure effects on the critical temperature have been found to lead to vastly different behaviors depending on the system [67–69].

Lastly, we analyzed closely the superconductivity results presented by Yesudhas *et al* [10]. As illustrated in figure 6(b) of [10], the material only enters in a superconducting state with zero resistance at 19.5 GPa. Additionally, in the 5.7-19 GPa interval, there is a finite resistance (see figure 6(a) of [10]) which suggests that in this pressure range the system could be in a mixed state characteristic of a type-II superconductor [70]. This

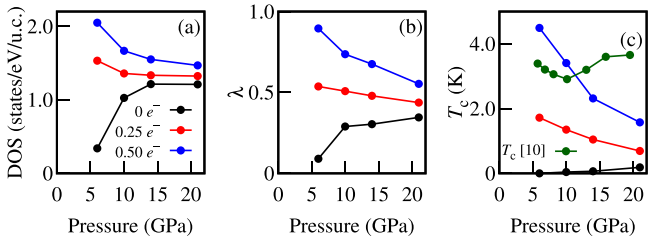


**Figure 7.** (a) DOS at the Fermi level, (b) electron-phonon coupling strength ($\lambda$), and (c) critical temperature ($T_c$) for pressures ranging from 0 to 21 GPa. The black, red, and blue circles correspond to calculations done with doping levels of 0, 0.25, and 0.5 electrons/u.c., respectively. The green circles correspond to the experimental onset $T_c$ data taken from [10].

latter observation is also supported by the resistance versus temperature curves for varying magnetic fields at 10.1 GPa in figure 6(c) of [10], showing that as the system goes in this mixed state, the resistance exhibits a gradual decrease as the temperature is lowered instead of a discontinuous drop to zero [70]. We also note that the V-shape pressure dependence of $T_c$ was obtained using the onset $T_c$ [10] (i.e., the temperature where the resistance starts to drop), while the calculated critical temperature corresponds to the zero-resistance $T_c$. Other factors, such as the appearance of competing electronic phases under pressure, non-hydrostatic pressure conditions in the experimental setup, and the presence of phase inhomogeneities in the sample, can also notably affect the critical temperature and may explain the discrepancy with theory [64, 71–74].

## 7. Conclusions

We performed an *ab initio* study to investigate the structural, electronic, vibrational, and superconducting properties of $TlInTe_2$ under pressure. Contrary to experiment, we did not find a V-shape $T_c$ behavior with pressure, and, in addition, the estimated $T_c$ is an order of magnitude smaller than the experimental values. Doping could, in principle, bring the $T_c$ within the experimental range, but the required doping levels are quite large. Furthermore, our calculations of the phonon spectra and phonon lifetimes with anharmonic effects demonstrate that anharmonicity is not expected to affect the superconducting properties of $TlInTe_2$. We conclude by asserting that further experimental and theoretical studies are required to elucidate not only the pressure range in which $TlInTe_2$ is superconducting and the dependence of $T_c$ with pressure, but also to explore whether other mechanisms may contribute to superconductivity in this system.

## Acknowledgments

The authors acknowledge support from the National Science Foundation (NSF) (Award No. DMR-2035518). This work used the Expanse system at the San Diego Supercomputer Center through allocation TG-DMR180071 from the Advanced Cyberinfrastructure Coordination Ecosystem: Services & Support (ACCESS) program [75], which is supported by NSF grants #2138259, #2138286, #2138307, #2137603, and #2138296. This study also used the Frontera supercomputer at the Texas Advanced Computing Center through the Leadership Resource Allocation (LRAC) award DMR22004. Frontera is made possible by NSF award OAC-1818253 [76]. We would also like to thank Chandan Setty and Alessio Zaccone for suggesting the project.

## Data availability statement

All data that support the findings of this study are included within the article (and any supplementary files).

## ORCID iDs

Christopher Renskers https://orcid.org/0009-0001-3662-0397
Elena R Margine https://orcid.org/0000-0002-5573-9940

## References

[1] Dutta M, Samanta M, Ghosh T, Voneshen D J and Biswas K 2021 Evidence of highly anharmonic soft lattice vibrations in a zintl rattler *Angew. Chem. Int. Ed.* **60** 4259–65

[2] Dutta M, Matteppanavar S, Prasad M V D, Pandey J, Warankar A, Mandal P, Soni A, Waghmare U V and Biswas K 2019 Ultralow thermal conductivity in chain-like tlse due to inherent $Tl^{+}$ Rattling *JACS* **141** 20293–9
[3] Ghafari A and Habicht K 2019 Electronic structure and transport properties of $TlInSe_2$ and $Tl_{0.5}Li_{0.5}InSe_2$ *Materials Today Energy* **12** 95–106
[4] Panich A M 2008 Electronic properties and phase transitions in low-dimensional semiconductors *J. Phys. Condens. Matter* **20** 293202
[5] Jana M K, Pal K, Warankar A, Mandal P, Waghmare U V and Biswas K 2017 Intrinsic rattler-induced low thermal conductivity in Zintl Type $TlInTe_2$ *JACS* **139** 4350–3
[6] Mamedov N, Wakita K, Ashida A, Matsui T and Morii K 2006 Super thermoelectric power of one-dimensional $TlInSe_2$ *Thin Solid Films* **499** 275–8
[7] Ves S 1990 High pressure raman study of the chain chalcogenide $TlInTe_2$ *Physica Status Solidi (b)* **159** 699–706
[8] Jabarov S, Ismayilova N, Kozlenko D, Mammadov T, Mamedov N, Orudzhev H, Kichanov S, Mikailzade F, Kasumova E and Dang N 2021 Structural and elastic properties of $TlInSe_2$ at high pressure *Solid State Sci.* **111** 106343
[9] Mamedov N T, Jabarov S H, Kozlenko D P, Ismayilova N A, Seyidov M Y, Mammadov T G and Dang N T 2019 Neutron diffraction study of the crystal structure of $TlInSe_2$ at high pressure *Int. J. Mod. Phys.* B **33** 1950149
[10] Yesudhas S *et al* 2021 Structural, vibrational, and electronic properties of 1D-$TlInTe_2$ under high pressure: a combined experimental and theoretical study *Inorg. Chem.* **60** 9320–31
[11] Ding G, He J, Cheng Z, Wang X and Li S 2018 Low lattice thermal conductivity and promising thermoelectric figure of merit of Zintl type $TlInTe_2$ *J. Mater. Chem.* C **6** 13269–74
[12] Pal K, Xia Y and Wolverton C 2021 Microscopic mechanism of unusual lattice thermal transport in $TlInTe_2$ *NPJ Comput. Mater.* **7** 5
[13] Wu M, Enamullah and Huang L 2019 Unusual lattice thermal conductivity in the simple crystalline compounds $TlXTe_2(X = Ga, In)$ *Phys. Rev.* B **100** 075207
[14] Setty C, Baggioli M and Zaccone A 2021 Anharmonic theory of superconductivity in the high-pressure materials *Phys. Rev.* B **103** 094519
[15] Giannozzi P *et al* 2009 QUANTUM ESPRESSO: a modular and open-source software project for quantum simulations of materials *J. Phys. Condens. Matter* **21** 395502
[16] Giannozzi P *et al* 2017 Advanced capabilities for materials modelling with Quantum ESPRESSO *J. Phys. Condens. Matter* **29** 465901
[17] Thonhauser T, Cooper V R, Li S, Puzder A, Hyldgaard P and Langreth D C 2007 Van der waals density functional: self-consistent potential and the nature of the van der waals bond *Phys. Rev.* B **76** 125112
[18] Klimeš J, Bowler D R and Michaelides A 2011 Van der Waals density functionals applied to solids *Phys. Rev.* B **83** 195131
[19] Sabatini R, Küçükbenli E, Kolb B, Thonhauser T and de Gironcoli S 2012 Structural evolution of amino acid crystals under stress from a non-empirical density functional *J. Phys. Condens. Matter* **24** 424209
[20] Thonhauser T, Zuluaga S, Arter C A, Berland K, Schröder E and Hyldgaard P 2015 Spin signature of nonlocal correlation binding in metal-organic frameworks *Phys. Rev. Lett.* **115** 136402
[21] Berland K, Cooper V R, Lee K, Schröder E, Thonhauser T, Hyldgaard P and Lundqvist B I 2015 van der Waals forces in density functional theory: a review of the vdW-DF method *Rep. Prog. Phys.* **78** 066501
[22] Hamann D R 2013 Optimized norm-conserving Vanderbilt pseudopotentials *Phys. Rev.* B **88** 085117
[23] van Setten M, Giantomassi M, Bousquet E, Verstraete M, Hamann D, Gonze X and Rignanese G M 2018 The PseudoDojo: Training and grading a 85 element optimized norm-conserving pseudopotential table *Comput. Phys. Commun.* **226** 39–54
[24] Perdew J P, Burke K and Ernzerhof M 1996 Generalized gradient approximation made simple *Phys. Rev. Lett.* **77** 3865–8
[25] Monkhorst H J and Pack J D 1976 Special points for Brillouin-zone integrations *Phys. Rev.* B **13** 5188–92
[26] Methfessel M and Paxton A T 1989 High-precision sampling for Brillouin-zone integration in metals *Phys. Rev.* B **40** 3616–21
[27] Baroni S, de Gironcoli S, Dal Corso A and Giannozzi P 2001 Phonons and related crystal properties from density-functional perturbation theory *Rev. Mod. Phys.* **73** 515–62
[28] Wierzbowska M, de Gironcoli S and Giannozzi P 2005 Origins of low- and high-pressure discontinuities of $T_c$ in niobium arXiv:cond-mat/0504077
[29] Giustino F, Cohen M L and Louie S G 2007 Electron-phonon interaction using Wannier functions *Phys. Rev.* B **76** 165108
[30] Margine E R and Giustino F 2013 Anisotropic migdal-eliashberg theory using wannier functions *Phys. Rev.* B **87** 024505
[31] Poncé S, Margine E, Verdi C and Giustino F 2016 EPW: Electron-phonon coupling, transport and superconducting properties using maximally localized Wannier functions *Comput. Phys. Commun.* **209** 116–33
[32] Marzari N, Mostofi A A, Yates J R, Souza I and Vanderbilt D 2012 Maximally localized wannier functions: theory and applications *Rev. Mod. Phys.* **84** 1419–75
[33] Pizzi G *et al* 2020 Wannier90 as a community code: new features and applications *J. Phys. Condens. Matter* **32** 165902
[34] Errea I, Calandra M and Mauri F 2014 Anharmonic free energies and phonon dispersions from the stochastic self-consistent harmonic approximation: application to platinum and palladium hydrides *Phys. Rev.* B **89** 064302
[35] Jochym P T and Łażewski J 2021 High efficiency configuration space sampling–probing the distribution of available states *SciPost Phys.* **10** 129
[36] van Roekeghem A, Carrete J and Mingo N 2021 Quantum self-consistent ab-initio lattice dynamics *Comput. Phys. Commun.* **263** 107945
[37] Hellman O, Steneteg P, Abrikosov I A and Simak S I 2013 Temperature dependent effective potential method for accurate free energy calculations of solids *Phys. Rev.* B **87** 104111
[38] Bottin F, Bieder J and Bouchet J 2020 a-TDEP: temperature dependent effective potential for abinit—lattice dynamic properties including anharmonicity *Comput. Phys. Commun.* **254** 107301
[39] Tadano T and Tsuneyuki S 2015 Self-consistent phonon calculations of lattice dynamical properties in cubic $SrTiO_3$ with first-principles anharmonic force constants *Phys. Rev.* B **92** 054301
[40] Erba A, Maul J, Ferrabone M, Carbonnière P, Rérat M and Dovesi R 2019 Anharmonic vibrational states of solids from dft calculations. part i: description of the potential energy surface *J. Chem. Theory Comput.* **15** 3755–65
[41] Zacharias M and Giustino F 2016 One-shot calculation of temperature-dependent optical spectra and phonon-induced band-gap renormalization *Phys. Rev.* B **94** 075125
[42] Karsai F, Engel M, Flage-Larsen E and Kresse G 2018 Electron-phonon coupling in semiconductors within the GW approximation *New J. Phys.* **20** 123008
[43] Tadano T, Gohda Y and Tsuneyuki S 2014 Anharmonic force constants extracted from first-principles molecular dynamics: applications to heat transfer simulations *J. Phys. Condens. Matter* **26** 225402

[44] Oba Y, Tadano T, Akashi R and Tsuneyuki S 2019 First-principles study of phonon anharmonicity and negative thermal expansion in $ScF_3$ *Phys. Rev. Mater.* **3** 033601
[45] Hajinazar S, Thorn A, Sandoval E D, Kharabadze S and Kolmogorov A N 2021 Maise: construction of neural network interatomic models and evolutionary structure optimization *Comput. Phys. Commun.* **259** 107679
[46] Momma K and Izumi F 2011 Vesta 3 for three-dimensional visualization of crystal, volumetric and morphology data *J. Appl. Crystallogr.* **44** 1272–6
[47] Chang C and Zhao L D 2018 Anharmoncity and low thermal conductivity in thermoelectrics *Materials Today Physics* **4** 50–7
[48] Li J, Hu W and Yang J 2022 High-throughput screening of rattling-induced ultralow lattice thermal conductivity in semiconductors *JACS* **144** 4448–56
[49] Allakhverdiev K R, Mamedov T G, Shteinshreiber V E and Efendieva I K 1985 Fundamental absorption edge of TISe and $TlInTe_2$ crystals *Physica Status Solidi (b)* **127** K55–60
[50] Hanias M, Anagnostopoulos A, Kambas K and Spyridelis J 1989 On the non-linear properties of $TlInX_2$ (X=S, Se, Te) ternary compounds *Physica* B **160** 154–60
[51] Rabinal M K, Titus S S K, Asokan S, Gopal E S R, Godzaev M O and Mamedov N T 1993 Effect of high pressure on the electrical conductivity of $TlInX_2$ (X=Se, Te) layered semiconductors *Physica Status Solidi* B **178** 403–8
[52] Tran F and Blaha P 2009 Accurate band gaps of semiconductors and insulators with a semilocal exchange-correlation potential *Phys. Rev. Lett.* **102** 226401
[53] Orudzhev G S, Godzhaev É A, Kerimova R A and Allakhyarov É M 2006 Band structure and optical properties of the $TlInTe_2$ chain compound *Phys. Solid State* **48** 42–6
[54] Wakita K, Shim Y, Orudzhev G, Mamedov N and Hashimzade F 2006 Band structure and dielectric function of $TlInTe_2$ *Physica Status Solidi (a)* **203** 2841–4
[55] See Supplemental Material for figures S1-S8.
[56] Kawamura M 2019 Fermisurfer: Fermi-surface viewer providing multiple representation schemes *Comput. Phys. Commun.* **239** 197–203
[57] Sen S and Guo G Y 2020 Pressure induced Lifshitz transition in ThFeAsN *Phys. Rev. Mater.* **4** 104802
[58] Feng J *et al* 2022 Superconductivity induced by lifshitz transition in pristine $SnS_2$ under high pressure *The Journal of Physical Chemistry Letters* **13** 9404–10
[59] Shi X *et al* 2017 Enhanced superconductivity accompanying a Lifshitz transition in electron-doped FeSe monolayer *Nat. Commun.* **8** 14988
[60] Narayan D M *et al* 2023 Potential Lifshitz transition at optimal substitution in nematic pnictide $Ba_{1-x}Sr_xNi_2As_2$ *Science Advances* **9** eadi4966
[61] Ding Y *et al* 2019 Disappearance of superconductivity and a concomitant lifshitz transition in heavily overdoped $Bi_2Sr_2CuO_6$ superconductor revealed by angle-resolved photoemission spectroscopy *Chin. Phys. Lett.* **36** 017402
[62] Lifshitz I M 1960 Anomalies of electron characteristics in the high pressure region *Zhur. Eksptl'. i Teoret. Fiz.* **38** 5
[63] Ying J, Paudyal H, Heil C, Chen X J, Struzhkin V V and Margine E R 2018 Unusual pressure-induced periodic lattice distortion in $SnSe_2$ *Phys. Rev. Lett.* **121** 027003
[64] Kafle G P, Heil C, Paudyal H and Margine E R 2020 Electronic, vibrational, and electron-phonon coupling properties in $SnSe_2$ and $SnS_2$ under pressure *J. Mater. Chem.* C **8** 16404–17
[65] Dynes R C 1972 McMillan's equation and the $T_c$ of superconductors *Solid State Commun.* **10** 615–8
[66] Allen P B and Dynes R C 1975 Transition temperature of strong-coupled superconductors reanalyzed *Phys. Rev.* B **12** 905–22
[67] Hamlin J J 2015 Superconductivity in the metallic elements at high pressures *Physica C: Superconductivity and its Applications* **514** 59–76
[68] Shimizu K 2015 Superconductivity from insulating elements under high pressure *Physica C: Superconductivity and its Applications* **514** 46–9
[69] Lorenz B and Chu C W 2005 *High Pressure Effects on Superconductivity* ed A V Narlikar (Springer)
[70] Hirsch J E and Marsiglio F 2021 Nonstandard superconductivity or no superconductivity in hydrides under high pressure *Phys. Rev.* B **103** 134505
[71] Katano S, Nakagawa H, Matsubayashi K, Uwatoko Y, Soeda H, Tomita T and Takahashi H 2014 Anomalous pressure dependence of the superconductivity in noncentrosymmetric $LaNiC_2$: Evidence of strong electronic correlations *Phys. Rev.* B **90** 220508
[72] Wiendlocha B, Szczęśniak R, Durajski A P and Muras M 2016 Pressure effects on the unconventional superconductivity of noncentrosymmetric $LaNiC_2$ *Phys. Rev.* B **94** 134517
[73] Martin I, Podolsky D and Kivelson S A 2005 Enhancement of superconductivity by local inhomogeneities *Phys. Rev.* B **72** 060502
[74] Paudyal H, Poncé S, Giustino F and Margine E R 2020 Superconducting properties of $mote_2$ from ab initio anisotropic migdal-eliashberg theory *Phys. Rev.* B **101** 214515
[75] Boerner T J, Deems S, Furlani T R, Knuth S L and Towns J 2023 ACCESS: advancing innovation: NSF's advanced cyberinfrastructure coordination ecosystem: services & support *Practice and Experience in Advanced Research Computing, PEARC '23* (Association for Computing Machinery) pp 173–6
[76] Stanzione D, West J, Evans R T, Minyard T, Ghattas O and Panda D K 2020 Frontera: The evolution of leadership computing at the national science foundation *Practice and Experience in Advanced Research Computing* (ACM)